Effects of inner electrons on atomic strong-field-ionization dynamics

J. Rapp and D. Bauer

Institut für Physik, Universität Rostock, 18051 Rostock, Germany

The influence of inner electrons on the ionization dynamics in strong laser fields is investigated in a wavelength regime where the inner electron *dynamics* is usually assumed to be negligible. The role of inner electrons is of particular interest for the application of frozen-core approximations and pseudopotentials in time-dependent density functional theory (TDDFT) and the single-active-electron (SAE) approximation in strong-field laser physics. Results of TDDFT and SAE calculations are compared with exact ones obtained by the numerical *ab initio* solution of the three-electron time-dependent Schrödinger equation for a lithium model atom. It is found that dynamical antiscreening, i.e., a particular form of dynamical core polarization, may substantially alter the ionization rate in the single-photon regime. Requirements for the validity of the approximations in the single and multiphoton ionization domain are identified.

I. INTRODUCTION

Density functional theory (DFT) simulations (see, e.g., [1–3]) have become popular tools for electronic structure calculations. Compared to the exact solution of the many-body Schrödinger equation, discrepancies in the electron density obtained from DFT-based Kohn-Sham (KS) [4] schemes are, by construction, caused by the unavoidable approximation to the generally unknown exact exchange-correlation (XC) potential. However, in practice it is common to apply additional approximations, most notably "pseudopotentials" or the "frozen-core approximation" (see, e.g., [5,6]) in order to avoid the numerical effort of treating tightly bound inner electrons. The justification for this neglect is that core electrons do not take directly part in, e.g., the formation of bonds.

DFT has been extended to systems in time-dependent external potentials. In principle, time-dependent density functional theory (TDDFT) (see, e.g., [7,8]) allows one to study many-electron systems such as atoms, molecules, or clusters in strong laser fields, even beyond linear response. It is known, however, that switching from DFT to TDDFT makes the unknown exact XC functional even more inaccessible because of memory effects and the initial-state dependence it should contain [8–12] but all practicable approximations to it do not.

In this paper, we study inner-electron dynamics induced by time-dependent external fields. In contrast to typical applications of DFT concerning the ground state electronic structure of the system at hand, even the lowest KS orbitals may undergo a significant modification if the system is subjected to a strong external laser field in TDDFT beyond linear response. Evidently, it is invalid to freeze those KS orbitals which directly contribute to, e.g., the outgoing electron density of an atom being ionized. If, on the other hand, solely the KS valence orbital dominates ionization, it is an eligible question if the essential dynamics can be reproduced by a frozen-core, pseudo-, or single-active-electron (SAE) potential. In fact, the SAE approximation is ubiquitous in the strong-field-ionization community (see, e.g., [13–16]). Only recently it has been recognized that in multielectron molecules it is often not permissible to consider only the highest occupied molecular orbital in strong-field processes [17,18].

The question we address in this paper is whether core electrons in atoms can be considered "frozen" or not in the interaction with *long* wavelength radiation. Here, "long" means that the photon energy $\hbar\omega$ should be small compared to the energy by which the core electrons are bound. Given the energy level spacings of the Li atom, we thus need to consider the multiphoton regime, and the single-photon regime up to photon energies well below values where the core electrons are accessed "directly" by the applied laser field.

We employ a model Li atom, for which we are able to numerically solve the time-dependent Schrödinger equation (TDSE) *ab initio*. Lithium is the simplest element with core electrons in the ground state configuration and thus serves as a perfect testing ground. However, strong-laser-driven Li in full dimensionality is well beyond present-day computational capabilities. Even with the spatial degrees of freedom restricted to one dimension (i.e., the laser polarization direction) per electron, the numerical demand is enormous for strong laser fields. We have been able to speed up the calculations by employing properties of the time-dependent, spatial three-body wave function in the ionization regime considered and by optimizing the TDSE solver for graphics processing units.

The paper is organized as follows. In Sec. II the Li model system is described. In Sec. III the methods and approximations used in this work are introduced. Results are presented in Sec. IV, and a conclusion and outlook are given in Sec. V. Remarks on numerical details are included as an Appendix. Atomic units (a.u.) are used throughout.

II. ONE-DIMENSIONAL LITHIUM MODEL

The Li atom is the simplest atom with "inner" and "outer" electrons in the ground state configuration. The reduction to one dimension per electron is required for the exact numerical treatment, as the computational effort grows exponentially with both particle number and dimension. One-dimensional atom models have been successfully used in the case of helium for more than 20 years [19] and more recently for Li as well [20].

Applying the dipole approximation, the Hamiltonian in length gauge reads

$$H(t) = \sum_i \left(T^{(i)} + V^{(i)} + H_L^{(i)}(t) + \frac{1}{2} \sum_{j \neq i} W^{(ij)} \right) \quad (1)$$

with indices $i, j \in \{1, 2, 3\}$, the kinetic energy operator

$$T^{(i)} = \tfrac{1}{2}(p^{(i)})^2, \quad (2)$$

the core potential

$$V^{(i)} = -Z[(x^{(i)})^2 + \varepsilon^2]^{-1/2}, \quad Z = 3, \quad (3)$$

the coupling to the laser field

$$H_L^{(i)}(t) = \mathcal{E}(t) x^{(i)}, \quad \mathcal{E}(t) = -\hat{\mathcal{E}} \sin \omega t, \quad (4)$$

and the electron-electron interaction operator $W^{(ij)}$,

$$W^{(ij)} = [(x^{(i)} - x^{(j)})^2 + \varepsilon^2]^{-1/2}. \quad (5)$$

The smoothing parameter $\varepsilon = 0.5034$ is tuned such that the total energy of the "real," three-dimensional Li atom is reproduced.

III. METHODS AND APPROXIMATIONS

In this section, we introduce the three methods used (TDSE, Floquet, and TDDFT) and the various approximations (frozen-core, pseudopotentials, and SAE). Particular emphasis is put on the structure of the three-electron wave function, which can be decomposed into a sum of three terms, each factorizing in a spin and a spatial part.

A. Time-dependent Schrödinger equation

The TDSE

$$i \partial_t |\Psi(t)\rangle = H(t) |\Psi(t)\rangle \quad (6)$$

is the fundamental equation describing the nonrelativistic time evolution of a many-particle quantum state $|\Psi(t)\rangle$. Due to the unavailability of an analytical solution for the Hamiltonian (1) we solve the TDSE numerically. In that way exact benchmark results are obtained to which results from approximate approaches will be compared.

1. Three-electron state $|\Psi(t)\rangle$

Let us expand the state $|\Psi(t)\rangle$ in orthonormal single-particle states

$$\{|n\rangle\}_{n \in \mathbb{N}}, \quad |n\rangle = |\phi_n\rangle \otimes |\chi_n\rangle, \quad (7)$$

where $|\phi_n\rangle$ and $|\chi_n\rangle$ are spatial and spin components, respectively. Suppressing the time argument, the expansion for three particles reads

$$|\Psi\rangle = \sum_n \left[\left(\sum_k a_{kn} |k\rangle^{(1)} \right) \right.$$

$$\left. \otimes \left(\sum_l b_{ln} |l\rangle^{(2)} \right) \otimes \left(\sum_m c_{mn} |m\rangle^{(3)} \right) \right] \quad (8)$$

$$= |ABC\rangle. \quad (9)$$

For brevity, the $\otimes$ sign denoting the tensor product will be omitted from now on. The shorthand notation (9) allows one to concisely formulate the correct exchange antisymmetry in the case of fermions:

$$|ABC\rangle = -|ACB\rangle = |CAB\rangle$$
$$= -|BAC\rangle = |BCA\rangle = -|CBA\rangle. \quad (10)$$

The antisymmetry (10) can be enforced on a general three-particle state $|A'B'C'\rangle$ by the antisymmetrization operator $\mathcal{A}$,

$$|\Psi\rangle = |ABC\rangle = \mathcal{N}' \mathcal{A} |A'B'C'\rangle, \quad (11)$$

where the normalization factor $\mathcal{N}'$ has to be chosen such that $\langle \Psi | \Psi \rangle = 1$, and

$$\mathcal{A} |A'B'C'\rangle = \frac{1}{3!} \big(|A'B'C'\rangle - |A'C'B'\rangle + |C'A'B'\rangle$$
$$- |B'A'C'\rangle + |B'C'A'\rangle - |C'B'A'\rangle \big).$$

Introducing the abbreviation $|x\sigma\rangle = |x_1\rangle|\sigma_1\rangle|x_2\rangle|\sigma_2\rangle|x_3\rangle|\sigma_3\rangle$, the expansion of $|\Psi\rangle$ in position-spin space reads

$$|\Psi\rangle = \sum_{\sigma_1 \sigma_2 \sigma_3} \iiint dx_1 dx_2 dx_3 \, |x\sigma\rangle \langle x\sigma | \mathcal{N}' \mathcal{A} |A'B'C'\rangle. \quad (12)$$

The configuration is chosen such that the total spin is $S = 1/2$ and $M_S = +1/2$ at all times. This can be justified by the fact that interaction Hamiltonians that could induce spin flips are not considered in this paper. The primed state $|A'B'C'\rangle$ can be chosen to have separable spin components, e.g., the corresponding expansion coefficients a'_{kn} are only nonvanishing for spin down while the other two coefficients always result in spin up. As a consequence, the function

$$\Psi(x_1, x_2, x_3) = \sum_{\sigma_1 \sigma_2 \sigma_3} |\sigma\rangle \langle x\sigma | \mathcal{N}' \mathcal{A} |A'B'C'\rangle \quad (13)$$

can be written as

$$\Psi(x_1, x_2, x_3) = \frac{\mathcal{N}'}{3!} \{ |\downarrow\uparrow\uparrow\rangle [\phi(x_1, x_2, x_3) - \phi(x_1, x_3, x_2)]$$
$$+ |\uparrow\downarrow\uparrow\rangle [\phi(x_2, x_3, x_1) - \phi(x_2, x_1, x_3)]$$
$$+ |\uparrow\uparrow\downarrow\rangle [\phi(x_3, x_1, x_2) - \phi(x_3, x_2, x_1)] \}, \quad (14)$$

with correlated spatial functions $\phi(x_1, x_2, x_3) = \sum_{klmn} a'_{kn} b'_{ln} c'_{mn} \langle x_1 | \phi_k \rangle \langle x_2 | \phi_l \rangle \langle x_3 | \phi_m \rangle$. Defining

$$\phi_{23}(x_1, x_2, x_3) = \mathcal{N}''[\phi(x_1, x_2, x_3) - \phi(x_1, x_3, x_2)], \quad (15)$$

which is antisymmetric with respect to the exchange of its second and third arguments, one obtains the compact form

$$\Psi(x_1, x_2, x_3) = \mathcal{N}[|\downarrow\uparrow\uparrow\rangle \phi_{23}(x_1, x_2, x_3)$$
$$+ |\uparrow\downarrow\uparrow\rangle \phi_{23}(x_2, x_3, x_1)$$
$$+ |\uparrow\uparrow\downarrow\rangle \phi_{23}(x_3, x_1, x_2)], \quad (16)$$

where $\mathcal{N} = \frac{\mathcal{N}'}{\mathcal{N}'' 3!}$. The full three-electron state $|\Psi\rangle$ is—at all times—completely determined by ϕ_{23},

$$|\Psi\rangle = \mathcal{N}[1 + \mathcal{P}^{(12)} \mathcal{P}^{(23)} + \mathcal{P}^{(23)} \mathcal{P}^{(12)}] |\downarrow\uparrow\uparrow\rangle |\phi_{23}\rangle. \quad (17)$$

Here, $P^{(ij)}$ is the two-particle permutation operator which exchanges the indices of particles i and j, and

$$|\phi_{23}\rangle = \iiint dx_1 dx_2 dx_3 |\boldsymbol{x}\rangle \phi_{23}(x_1, x_2, x_3). \qquad (18)$$

We assume that $|\phi_{23}\rangle$ is normalized to unity, $\langle \phi_{23} | \phi_{23}\rangle = 1$, so that $\mathcal{N} = \frac{1}{\sqrt{3}}$.

2. Spatial TDSE

Inserting a time-dependent state $|\Psi(t)\rangle$ of the form (17) into the TDSE (6) yields

$$[1 + \mathcal{P}^{(12)}\mathcal{P}^{(23)} + \mathcal{P}^{(23)}\mathcal{P}^{(12)}][i\partial_t - H(t)]|{\downarrow}{\uparrow}{\uparrow}\rangle|\phi_{23}(t)\rangle = 0 \qquad (19)$$

because both ∂_t and $H(t)$ commute with any two-particle permutation operator $\mathcal{P}^{(ij)}$.

Assuming a spin-diagonal Hamiltonian, multiplication of (19) from the left by, e.g., $\langle {\downarrow}{\uparrow}{\uparrow}|$, yields a TDSE for the evolution of $|\phi_{23}(t)\rangle$ in time,

$$i\partial_t |\phi_{23}(t)\rangle = \langle {\downarrow}{\uparrow}{\uparrow}| H(t) |{\downarrow}{\uparrow}{\uparrow}\rangle |\phi_{23}(t)\rangle. \qquad (20)$$

Although the Hamiltonian (1) does not act on spin components at all, the TDSE (20) still holds for spin-diagonal Hamiltonians. This will be utilized in Sec. IV C. The TDSE (20) is the one that is actually solved numerically in position space on a discretized $x_1 x_2 x_3$ grid. More details about the numerical solution are described in the Appendix.

3. Observables for both spin projections

Although electrons are indistinguishable, the partial wave function ϕ_{23} allows one to extract information about inner and outer electrons separately. Given a one-particle operator $a^{(i)}$ acting on the spatial component only, one can construct a spin-spatial operator a_σ of the form

$$a_\sigma = \sum_i |\sigma\rangle^{(i)} \langle\sigma|^{(i)} a^{(i)}, \qquad (21)$$

where

$$|\sigma\rangle^{(1)} \langle\sigma|^{(1)} = \sum_{\sigma_1 \sigma_2} |\sigma\rangle |\sigma_1\rangle |\sigma_2\rangle \langle\sigma| \langle\sigma_1| \langle\sigma_2|,$$

$$|\sigma\rangle^{(2)} \langle\sigma|^{(2)} = \sum_{\sigma_1 \sigma_2} |\sigma_1\rangle |\sigma\rangle |\sigma_2\rangle \langle\sigma_1| \langle\sigma| \langle\sigma_2|,$$

$$|\sigma\rangle^{(3)} \langle\sigma|^{(3)} = \sum_{\sigma_1 \sigma_2} |\sigma_1\rangle |\sigma_2\rangle |\sigma\rangle \langle\sigma_1| \langle\sigma_2| \langle\sigma|.$$

The choice of either $|\sigma\rangle = |{\downarrow}\rangle$ or $|\sigma\rangle = |{\uparrow}\rangle$ then yields an operator for calculating observables for the *single spin-down inner electron* on the one hand and for the *two spin-up electrons* on the other hand, respectively. The latter will be referred to as *inner-outer spin component* [21].

4. Ionization

The ionization probability is chosen as the primary observable for our investigations because it is well defined and comparable among all considered methods. In the TDSE simulation, position space (x_1, x_2, x_3) is divided into four regions, differing by the number of electrons which are
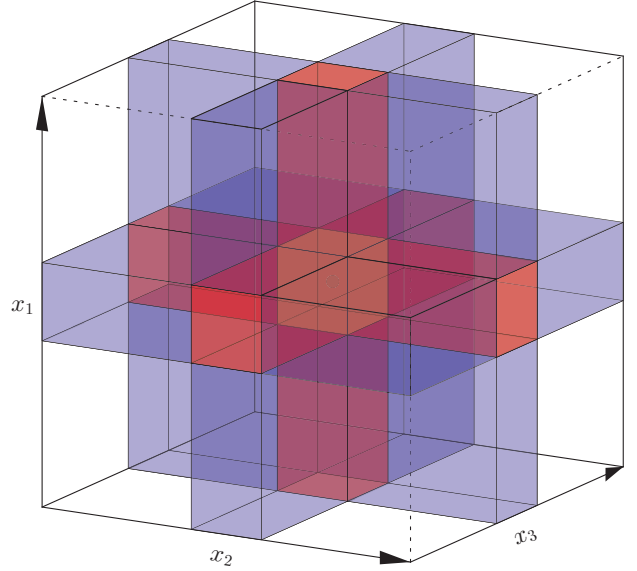

FIG. 1. (Color online) Schematic view of a cubic simulation box around the nucleus in the center. Different colors indicate those regions where zero (neutral Li), one (Li$^+$), two (Li^{2+}), or all three electrons (Li^{3+}) are located at positions far from the nucleus, respectively.

located far away from the nucleus (see Fig. 1). The respective ionization regions are (i) no ionization: single small cube around the nucleus; (ii) single ionization: six channels pointing to the surface centers of the simulation box; (iii) double ionization: twelve cuboids, four lying in each of the three central plains; and (iv) triple ionization: eight cubes in the corners of the simulation box.

The laser parameters considered throughout this paper are such that multiple ionization is negligible. Thus, the (single-) ionization probability $p(t)$ reduces to $p(t) = 1 - N(t)$ where $N(t)$ is the norm inside the cube around the nucleus (representing neutral Li).

B. Floquet method

The whole purpose of applying the Floquet approach in this work is the determination of resonances, taking the ac Stark effect into account.

In general, the Floquet method (see, e.g., [22,23]) allows one to study time-dependent problems without an explicit time propagation. This is possible if the Hamiltonian $H(t)$ is periodic in time, i.e.,

$$H(t) = H_0 + H_L(t), \quad H_L(t + T) = H_L(t), \qquad (22)$$

because the so-called Floquet theorem then allows one to obtain a time-independent eigenvalue equation for the field-dressed states and the corresponding quasienergies. Quasienergy spectra are useful for predicting resonance enhancements in the ionization rate as a function of the laser frequency with the ac Stark effect automatically included. The Floquet method will thus be used to follow the quasienergies $\epsilon_m^{(n)}$ for varying photon energies ω and a fixed electric field amplitude $\hat{\mathcal{E}}$. Here, the index $m \in \mathbb{N}$ refers to the (unperturbed)

atomic energy level, and the index $n \in \mathbb{Z}$ to the "Floquet block" (note that $\epsilon_m^{(n)} + \omega = \epsilon_m^{(n+1)}$).

C. Time-dependent density functional theory

DFT [1–3] and its time-dependent extension TDDFT [7,8] are approaches to overcome the exponential scaling of the numerical effort with the number of particles. They are based on the fact that all information about the system is included in the (time-dependent) single-particle density $n(x)$, as proven by the Hohenberg-Kohn theorem [24] and its time-dependent analog, the Runge-Gross theorem [25]. (TD)DFT calculations are performed in practice within a KS scheme, i.e., the single-particle density is reproduced with the help of a fictitious, much easier-to-solve noninteracting system evolving in an effective KS potential.

In this work, the spin-polarized Li system is studied. We therefore consider the spin densities $n_\sigma(x)$, $\sigma \in \{\downarrow, \uparrow\}$. The exchange-only local-spin-density approximation (LDA) is employed for the XC functional. The exchange functional for the three-dimensional electron gas is considered because the one-dimensional model introduced in Sec. II is meant to mimic a three-dimensional three-electron atom in a linearly polarized laser field rather than a true one-dimensional system.

The time-dependent KS equation reads (spatial arguments suppressed)

$$i\partial_t \varphi_i(t) = H_{\mathrm{KS}}^{(\sigma_i)}(t) \varphi_i(t) \qquad (23)$$

with the KS Hamiltonian

$$H_{\mathrm{KS}}^{(\sigma_i)}(t) = -\frac{1}{2}\frac{\partial^2}{\partial x^2} + v(t) + v^{(\mathrm{H})}[n(t)] + v^{(\mathrm{XC})}[n_{\sigma_i}(t)] \quad (24)$$

and $n_\sigma(t) = \sum_i n_i(t)\,\delta_{\sigma_i \sigma}$, $n_i(t) = |\varphi_i(t)|^2$, $n(t) = \sum_\sigma n_\sigma(t)$. The same external potential $v(t)$ as in the many-body TDSE (i.e., binding potential plus laser in our case) appears here, $v^{(\mathrm{H})}$ is the Hartree potential, and $v^{(\mathrm{XC})}$ is the XC potential (to be approximated).

A known problem of LDA is the wrong asymptotic behavior of the KS potential $v + v^{(\mathrm{H})} + v^{(\mathrm{XC})}$. Each KS orbital in an, e.g., unperturbed, neutral atom should experience a potential $-1/r$ far away from the nucleus, representing one unscreened nuclear charge. This correct behavior can be enforced by the so-called Perdew-Zunger (PZ) self-interaction correction (SIC) [26]. PZ SIC corrects the Hartree and XC potentials for each orbital i by subtracting the potentials evaluated for the "own" single-particle density n_i. In the case of PZ-corrected LDA, the final corrected XC potential is calculated as (time and space arguments suppressed)

$$v_i^{(\mathrm{LDA+PZ})} = v^{(\mathrm{LDA})}[n_{\sigma_i}] - v^{(\mathrm{H})}[n_i] - v^{(\mathrm{LDA})}[n_i]. \quad (25)$$

It is easy to see that this leads to the correct SIC in the single-electron limit. However, due to the nonlinearity of the KS potential, i.e., $v^{(\mathrm{XC})}[n] - v^{(\mathrm{XC})}[n_i] \neq v^{(\mathrm{XC})}[n - n_i]$, the self-interaction is not completely removed by PZ SIC in general. The PZ-corrected KS Hamiltonian is orbital dependent, i.e., it is in general different for each orbital i (i.e., not only different for orbitals with different σ_i, as in "conventional" spin-DFT). An unpleasant consequence of this orbital dependence of the KS Hamiltonian is the nonorthogonality of the PZ-SIC KS orbitals (although in practice they are usually very close to

orthogonal). Positive consequences of the PZ SIC are that, besides the correct asymptotic behavior of potentials and densities, the values for the total energy, and ionization energies (or electron affinities of negative ions) typically improve.

D. Frozen-core approximation

All-electron (TD)DFT calculations often become numerically too demanding. Hence, it is common to apply additional approximations in order to reduce the numerical effort further. One may employ the fact that chemical bonds and reactions are governed by valence electrons so that the relaxation of electronic core shells may be considered negligible. Consequently, tightly localized KS orbitals may be self-consistently determined for the initial state configuration but "frozen" during the actual TDDFT time propagation. This approach will be referred to as "frozen-core approximation" (FCA). One of the issues in this work is the validity of the FCA for atoms interacting with a strong laser field, i.e., in TDDFT calculations beyond linear response.

E. Pseudopotentials

Consider a one-dimensional (e.g., radial) KS orbital, which is orthogonal to n other mutually orthogonal orbitals. If these other orbitals are constructed with the minimum number of nodes the considered orbital must have at least n nodes. A numerical grid thus requires a fine spatial resolution in order to resolve all orbital nodes, including the behavior in-between where the second derivative can reach high absolute values.

A popular tool which aims at circumventing the numerical demand caused by orbitals with many, densely distributed nodes are "pseudopotentials" (see, e.g., [5,6]). After applying the FCA, an artificial potential is constructed such that those orbitals which are not frozen yield the same single-particle density outside a certain cutoff radius r_{c} as in the full calculation but have less nodes within $[0, r_{\mathrm{c}}]$. Moreover, the pseudopotential is "designed" to reproduce the KS energies of the unfrozen orbitals (and possibly also those of the unpopulated, excited states). As in the motivation of the FCA, the argument for using pseudopotentials in chemistry is that only valence electron densities are important for the questions of interest such as molecular binding properties and chemical reactions. In other words, only the electron density far away from the nuclei is important.

In the hierarchy of approximations, pseudopotentials reside below the FCA. Hence we do not test particular pseudopotentials in this work. If the FCA fails, pseudopotentials will fail too (unless there is a lucky cancellation of errors caused by the removal of the nodes for $r < r_{\mathrm{c}}$).

F. Single-active-electron approximation

In the SAE picture it is assumed that the electron under investigation can be described as a single particle moving in an effective, external potential. It thus may be also viewed as an FCA. DFT provides one option to approximate this effective, external potential: one performs an all-electron DFT calculation for the desired initial electron configuration (usually the ground state) and subsequently "freezes" all KS orbitals but the one for the SAE of interest for the

real-time propagation [27]. In that way, a dependence on the XC potential is introduced only indirectly through the initial state. In the strong-field community, often simple analytical expressions for screened Coulomb potentials with adjustable screening parameters are used [28,29].

The question arises as to which state the SAE should populate in the effective potential. Common choices are (i) the ground state (corresponding to a pseudopotential approach with one valence electron) or (ii) some excited state (corresponding to pure FCA). The latter choice is more relevant for applications to intense laser-atom interaction, as the orbital symmetry of the initial state of the valence electron is important and can be measured in ionization experiments [30]. We will therefore concentrate on this case.

IV. RESULTS

The results in this work are organized as follows. In Sec. IV A the lowest-lying stationary states of the model Li atom introduced in Sec. II are determined. Exact results for the ionization rate are considered in Sec. IV B in order to identify different mechanisms behind the ionization process for different regimes of laser parameters. In Sec. IV C, a *gedanken experiment* is performed, revealing the mechanisms by which seemingly passive "inner" electrons can influence the ionization probability of the "outer" electron. In Sec. IV D the exact results are compared with TDDFT in various approximations.

A. Stationary states

The highly optimized TDSE solver for propagating the full three-particle wave function (details in the Appendix) is used in the imaginary-time mode for calculating the unperturbed eigenstates of the model Li. The ground state energy is $E_0 = -7.4782$. As we are investigating single ionization in the present work, it is useful to determine the single-ionization continuum threshold. This can be done by comparing with the ground state of Li^+ or by following the Rydberg series of singly excited states E_m of the neutral Li towards E_∞, both leading to an ionization potential $E_{ip} = E_\infty - E_0 \simeq 0.375$. Table I lists the energies for the lowest eight excited states.

As an example, Fig. 10 in the Appendix shows a cut at $x_1 = 0$ of $|\phi_{23}(x_1, x_2, x_3)|^2$ for the seventh excited state. The single spin-down component is oriented spatially along x_1 in

TABLE I. Energies E_m of the energetically lowest eigenstates $m = 0, 1, 2, \ldots, 8$ of the Li model atom.

m	E_m
0	−7.4782
1	−7.2838
2	−7.2020
3	−7.1657
4	−7.1431
5	−7.1306
6	−7.1213
7	−7.1156
8	−7.1110

the partial wave function ϕ_{23}. As the spin-down component necessarily belongs to an inner electron, the extent of the probability density $|\phi_{23}|^2$ is small in the x_1 direction. Hence the cut at $x_1 = 0$. We further observe the antisymmetry plane $x_2 = x_3$ and the preference of spatial regions where no more than one electron is located at a position comparatively far from the nucleus.

B. Ionization in different laser regimes

The ionization rate Γ_ω for a certain photon energy ω was determined by fitting $N(t)$ to $p_\omega(t) \simeq 1 - \exp(-\Gamma_\omega t)$ [see the definition of $p(t)$ in Sec. III A 4] during the flat-top part of a trapezoidal laser pulse. Given a maximum simulation time $\tau \geqslant t \geqslant 0$, the electric field amplitude $\hat{\mathcal{E}}$ during the flat-top part of the pulse is chosen high enough to make the relevant ionization time scales for a "numerically measurable" ionization yield shorter than τ. Besides the inverse ionization rate Γ_ω^{-1}, also the inverse n-photon Rabi frequency $\Omega_{R,n}^{-1}$ matters here. On the other hand, the ponderomotive energy $U_p = \frac{\hat{\mathcal{E}}^2}{4\omega^2}$ should be smaller than both the ionization potential E_{ip} and the photon energy ω. Otherwise, (strong field) effects such as ac Stark shifts, above-threshold ionization, and stabilization [31] could influence the ionization dynamics dramatically [32]. The electric field amplitude was therefore set to $\hat{\mathcal{E}} = 0.05$.

It is obvious that FCAs fail for photon energies $\omega \gg E_{ip}$ high enough to produce core holes. Too low laser frequencies are numerically too demanding. Hence, the frequencies considered in this work are restricted to $\omega \in [0.1, 1.0]$. Within this regime we encounter single-photon ionization for $\omega \geqslant E_{ip}$ and multiphoton ionization for $\omega < E_{ip}$.

1. Ionization rates

Ionization rates Γ_ω obtained by the exact solution of the TDSE are shown in Fig. 2. As expected, one can qualitatively distinguish between the single-photon and multiphoton ionization regime.
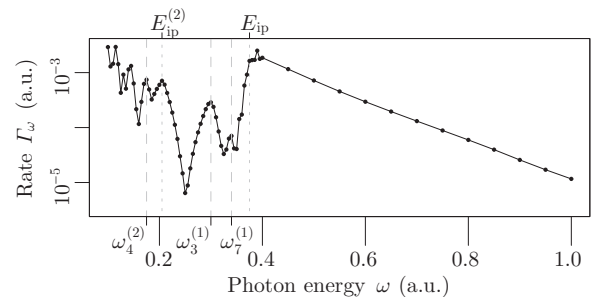

FIG. 2. Logarithmic plot of the ionization rate Γ_ω of the Li model atom vs the laser frequency ω for $\hat{\mathcal{E}} = 0.05$, as obtained from the *ab initio* solution of the TDSE. Ionization thresholds for one and two photons are given by the dotted, vertical lines. n-photon resonances with the mth excited state are denoted by $\omega_m^{(n)}$ (dashed, vertical lines). The regime of multiphoton ionization $\omega < E_{ip}$ is dominated by resonances at $\omega_m^{(n)}$ and $E_{ip}^{(2)}$ whereas the photoionization probability decreases exponentially (i.e., linearly on the logarithmic scale) for $\omega > E_{ip}$, starting at its maximum for $\omega \simeq E_{ip}$.

a. Single-photon ionization. If the photon energy increases beyond $\omega = E_{\mathrm{ip}}$, the ionization rate drops exponentially. Note that this behavior can only partially be explained by the decreasing number of photons per time and area for the fixed laser intensity in the simulation. In a simple picture, the ionization rate Γ_ω should be the product of the photoionization cross section $\sigma = \sigma(\omega)$ and the photon impact rate per area $\Gamma_{\mathrm{photon}}/A$. Hence one would expect $\Gamma_\omega = \sigma \Gamma_{\mathrm{photon}}/A = \sigma I/\omega$, where I denotes the (in our case constant) laser intensity. Instead, the almost linearly decreasing slope in the logarithmic plot of Γ_ω in Fig. 2 shows that Γ_ω is *not* $\sim \omega^{-1}$. Hence there must be an exponential dependence in $\sigma(\omega)$.

b. Multiphoton ionization. Peaks in the ionization rate Γ_ω for $\omega < E_{\mathrm{ip}}$ can be categorized into two groups. If the energy of n photons is just sufficient to free the outer electron, the ionization probability is particularly high. Consequently, one finds a peak just above the two-photon ionization threshold $E_{\mathrm{ip}}^{(2)} \simeq E_{\mathrm{ip}}/2$. However, the ac Stark shift increases for smaller laser frequencies ω. Thus, it becomes more important to consider field-dressed states in order to predict n-photon ionization thresholds for $n > 2$.

Another mechanism that leads to peaks in the multiphoton regime is excited-state-assisted ionization where (a) the energy of n photons matches the energy gap $E_m - E_0$ between the ground state and the mth excited state, (b) the n-photon transition between the ground state and the mth excited state is allowed, and (c) the binding energy $E_\infty - E_m$ of the mth excited state is smaller than the photon energy so that the absorption of one additional photon leads to ionization. This scenario may be viewed as n-photon Rabi oscillations, accompanied by ionization. Laser-dressed states have to be considered in order to precisely predict the peak positions $\omega_m^{(n)}$, especially for small laser frequencies.

2. Time-dependent ionization probability

Ionization just above any n-photon ionization threshold should depend solely on a single time scale given by the rate Γ_ω. Instead, in the case of excited-state-assisted ionization the ionization probability vs time should be modulated on the time scale of (multiphoton) Rabi floppings. This is indeed the case, as shown in Fig. 3 where the inverse ionization probability $1 - p_\omega(t)$ is plotted vs t for four values of the photon energy ω.

3. Position of resonance peaks

In order to quantitatively predict the position of the peaks in the ionization rate Γ_ω it is required to consider the ac Stark effect. The laser parameters used in this work are such that the coupling of the ground state to states with excited inner electrons is negligible. Hence, one can obtain Floquet spectra by considering states below the first ionization threshold only. The results of the Floquet solver are shown in Fig. 4.

a. Avoided crossings of the shifted ground state. Avoided crossings of the field-dressed ground state are of particular interest here because the system should be described by this state after an appropriate ramping of the laser field in the TDSE solution [33].

Following the perturbed ground state $m = 0$, $n = 0$ from the high-frequency limit to lower frequencies, one finds avoided crossings with the odd excited states $m \in \{9,7,5,3,1\}$
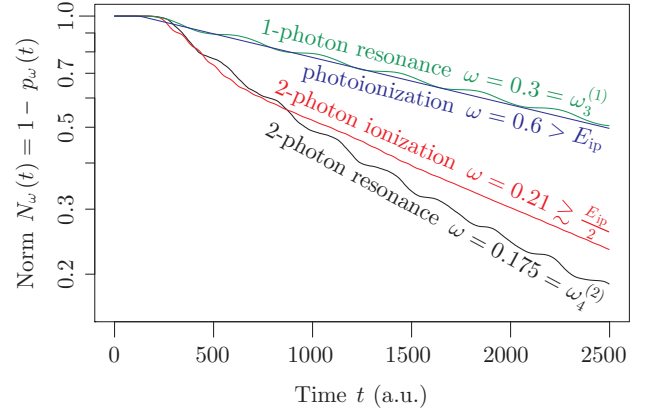

FIG. 3. (Color online) Comparison of time-dependent ionization probabilities $p_\omega(t)$ for photon energies $\omega \in \{0.175, 0.21, 0.3, 0.6\}$ and a fixed electric field amplitude $\hat{\mathcal{E}} = 0.05$, ramped over five cycles. In the case of resonances, i.e., excited-state-assisted ionization, the slope changes periodically with the Rabi frequency. In one- and two-photon ionization without excited-state assistance, the only relevant time scale is given by Γ_ω^{-1}, leading to a straight slope in the logarithmic plot (disregarding the transient behavior at small times t caused by laser ramping).

of the next lower Floquet block, as expected from the dipole selection rule. The minimum level distances in these one-photon avoided crossings are given by the Rabi frequency $\Omega_{\mathrm{R},1}$, which decreases for increasing m so that those for $m = 9$ and $m = 7$ are too close to be resolved. This is expected because $\Omega_{\mathrm{R},1}$ is proportional to the dipole transition amplitude, which decreases with increasing m.

Following in Fig. 4 $m = 0$, $n = 0$ below the two-photon ionization threshold $E_{\mathrm{ip}}^{(2)} \simeq 0.2$, two-photon avoided crossings of the ground state with even states $m = 8$ (unresolved), $m = 6$ (unresolved), $m = 4$ (hardly resolved), and $m = 2$ (clearly resolved) show up. In the case of n-photon crossings for $n \geqslant 3$, the identification of states becomes cumbersome, as Floquet blocks approach each other and the ac Stark shift increases.

b. Prediction of peaks in the ionization rate. In Fig. 4, photon energies with a high ionization rate are marked by dashed (excited-state-assisted ionization) and dotted (n-photon ionization thresholds) vertical lines. For each of these photon energies, the responsible mechanism can be identified by inspecting the behavior of the state $m = 0$, $n = 0$. The other way around it is not that straightforward. There are avoided crossings at photon energies $\omega_1^{(1)}$ and $\omega_5^{(1)}$ which do not give a significant peak in the ionization rate Γ_ω. However, for most of the avoided crossings one can quantitatively predict a peak position in the ionization rate, which is supporting the mechanisms introduced in Sec. IV B.

C. Coupling of inner electrons

In this section, a gedanken experiment is performed. Halfway between freezing the inner electrons and taking their dynamics fully into account lies a treatment where only their interaction with the laser is neglected while the electron-electron interaction W_{ij} is included in the simulation. However, switching off the interaction with the laser for both
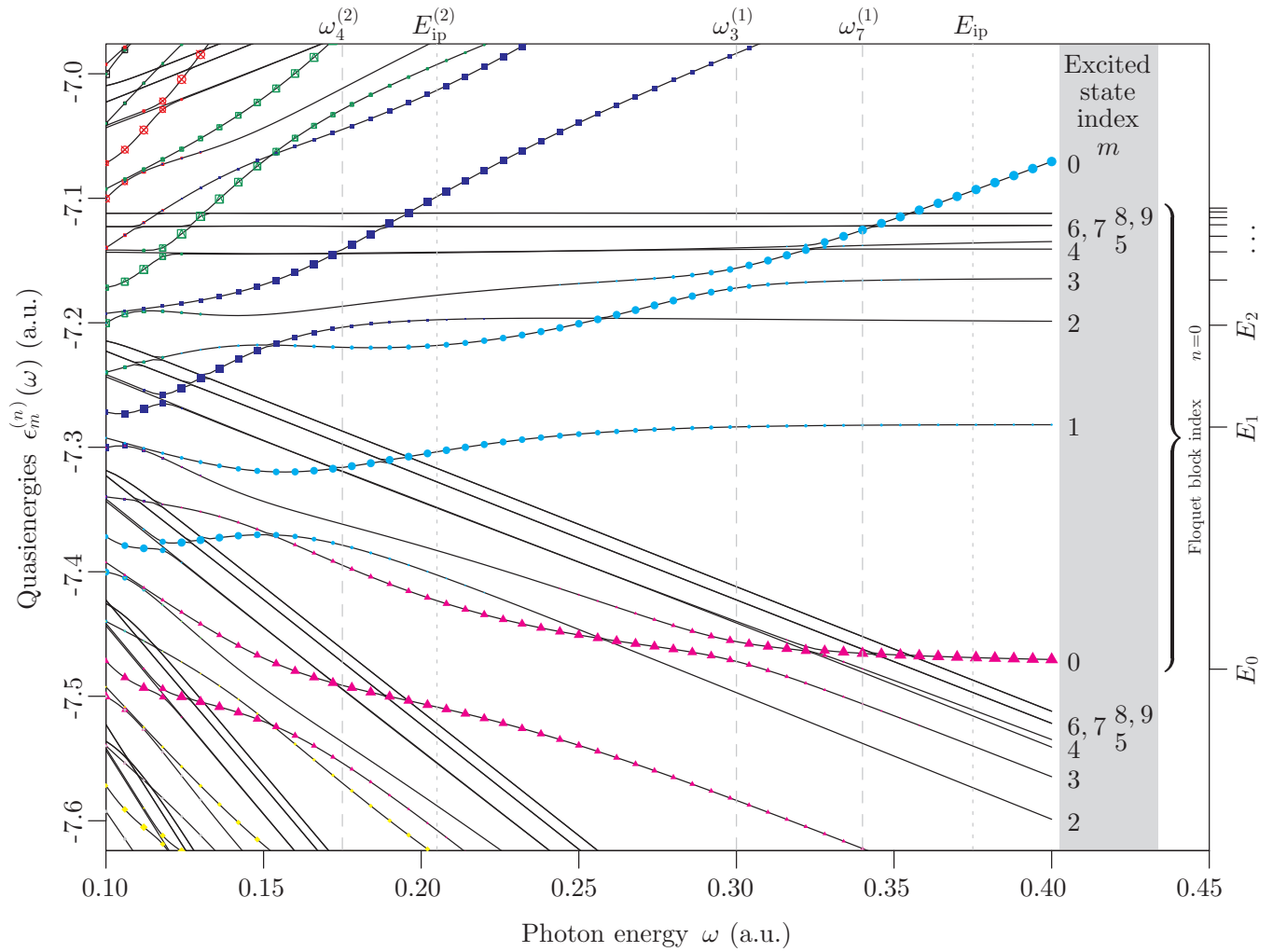
FIG. 4. (Color online) Quasienergies $\epsilon_m^{(n)}(\omega)$ of Floquet states vs photon energy ω for $\hat{\mathcal{E}} = 0.05$. Indices denote the state m and the Floquet block n. Those Floquet states with a sizable projection on the atomic ground state $m = 0$ are marked by symbols (shaped and colored differently for each Floquet block). Photon energies ω leading to a peak in the ionization rate Γ_ω are indicated by gray vertical lines, as in Fig. 2. The energies E_m with $m = 0,1,2$ on the right-hand side denote unperturbed atomic energy levels.

inner electrons is not possible in the exact TDSE calculation because this would break the exchange symmetry discussed in Sec. III A. An interaction that does not break the exchange symmetry is a "spin-selective laser" coupling $\sum_i H_L^{(i)}(t)$ with [see Eq. (21)]

$$H_L^{(i)}(t) = |{\uparrow}\rangle^{(i)}\, \langle{\uparrow}|^{(i)}\, \mathcal{E}(t)\, x^{(i)}. \tag{26}$$

When solving the TDSE (20) for ϕ_{23}, this hypothetical laser acts on all electrons except the single inner spin-down electron. In that way we can investigate the role of the (seemingly passive) inner spin-down electron during the ionization process by discriminating its reaction *only* to the spin-up electrons' laser-induced dynamics from its full interaction with *both* the laser and the other electrons.

1. Ionization rates

Ionization rates for the spin-selective case are compared with the previous full-laser results in Fig. 5. In the multiphoton ionization regime $\omega < E_{ip}$ both curves are in good agreement. Positions, heights, and widths of the peaks in both cases

match quantitatively. However, in the single-photon ionization regime $\omega \geqslant E_{ip}$ significant differences in the ionization rate are observed. Most notably, the ionization rate for the spin-selective laser is too high and shows a wrong asymptotic behavior with increasing frequency. Hence, the interaction of
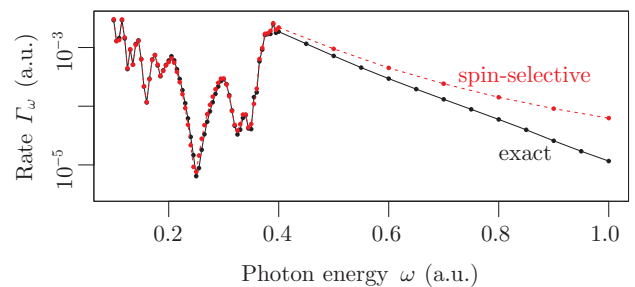

FIG. 5. (Color online) Ionization rate Γ_ω vs ω in the case of an artificial, spin-selective laser (dashed) compared to the previous results where all electrons "see" the laser (solid).

inner electrons with the laser field affects the ionization rate even though all inner electrons stay bound.

2. Dipole expectation values in the laser-driven case

The excursions of loosely outer and tightly inner bound electrons driven by an oscillating electric field $\mathcal{E}(t) = -\hat{\mathcal{E}}\sin(\omega t)$ are expected to be opposite in phase if the laser period falls in between their respective time scales. In a harmonic binding potential, for example, the phase depends on the sign of $\omega_0^2 - \omega^2$ with ω_0 the eigenfrequency of the harmonic potential. In the case of a high-frequency driver $\frac{\omega_0}{\omega} < 1$ the electron is displaced opposite to the driving force $-\hat{\mathcal{E}}(t)$. On the other hand, a bound electron with a faster time scale than the driver, $\frac{\omega_0}{\omega} > 1$, is displaced in the direction of the driving force. In terms of inner and outer electrons this means that the position expectation value of an outer electron is more likely to oscillate in phase with the electric field, whereas inner electrons tend to have the opposite phase. Note that "in phase with the electric field" means "opposed to the force" due to the negative charge of the electron. Time-dependent position expectation values for both spin components of the Li model interacting with a ramped sinusoidal laser field are shown in Fig. 6. Results were obtained for the case of an "ordinary" laser on the one hand and for the case of the artificial spin-selective laser on the other hand.

The amplitude of the single spin-down inner electron is one order of magnitude smaller than the amplitude of the inner-outer spin component. It is thus a good approximation to assign the position expectation value of the inner-outer spin component to the outer electron. As predicted by the harmonic oscillator the loosely bound outer electron oscillates in phase with the electric field, whereas the inner spin-down electron oscillates with the opposite phase.

The comparison of position expectation values for ordinary and spin-selective lasers shows that switching off the laser for the single spin-down inner electron does not affect the oscillation amplitude of the outer electron (see both bold curves on top of each other in Fig. 6). In contrast, the amplitude for the single spin-down inner electron itself decreases by a factor of 2 if the ordinary laser (thin solid black) is replaced by the spin-selective (thin dashed red) laser.

In the case of the spin-selective laser, the single spin-down inner electron oscillates with the laser frequency ω although it is not directly interacting with the laser. It only couples indirectly to the laser field via the electron-electron interaction $W^{(ij)}$. Both spin-up electrons are directly coupled to the laser field and repel the spin-down electron. The latter is therefore slightly displaced in the direction of the electric field by the other inner electron and in the opposite direction by the outer electron. The net result for the quantum mechanical expectation value is an excursion in the opposite direction (thin dashed red), but less so as if it were "seeing" the laser as well (thin solid black).

As proven by the significantly differing single-photon ionization rates in the gedanken experiment, the coupling between inner and outer electrons strongly affects the ionization process despite a seemingly harmless approximation: Only the laser interaction of one of the inner electrons is neglected. One can think of the decrease in the ionization rate in the full simulation as *dynamical antiscreening* of the nuclear charge. This is a particular form of dynamical core polarization, which could be modeled by adding a polarization potential to the SAE Hamiltonian (see, e.g., [34,35]).

One might wonder why the ionization rate is so different for the two laser types in Fig. 5 while the position expectation values for the inner-outer spin component in Fig. 6 are virtually equal. The explanation is that the position expectation values are dominated by the bound part of the wave function while the ionization rate is determined by the (small) escaping (and numerically absorbed) part.

3. Polarization by a constant electric field

In the limit $\frac{\omega_0}{\omega} \gg 1$ a dipole expectation value $x_\sigma(\mathcal{E}_0) = \langle \Psi(\mathcal{E}_0)|x_\sigma|\Psi(\mathcal{E}_0)\rangle$ with the sign opposite to $\mathcal{E}_0$ is expected for both spin components if the electrons were noninteracting. However, the electron-electron interaction $W^{(ij)}$ modifies this.

The numerical results in Fig. 7 support the picture of inner electrons reacting to the displacement of the outer electron. The expectation value of the single spin-down inner electron $x_\downarrow(\mathcal{E}_0)$ has the same sign as the electric field $\mathcal{E}_0$.
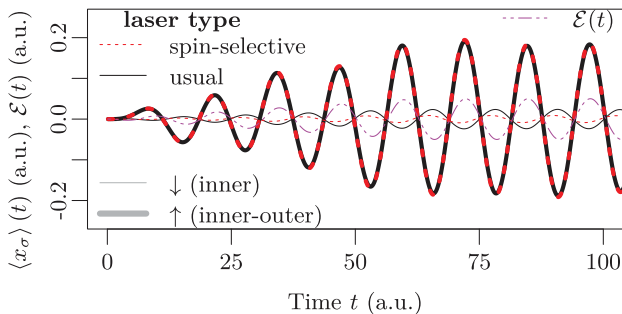

FIG. 6. (Color online) Time-dependent position expectation value of the spin-down component $x_\downarrow(t)$ (inner electron; thin) compared with the position expectation value of the other spin component $x_\uparrow(t)$ (inner and outer electrons; bold). The sinusoidal electric field $\mathcal{E}(t)$ with frequency $\omega = 0.5$ (thin dashed-dotted, purple) is ramped over five periods and interacts either with all electrons (usual case; solid) or with all electrons except the single spin-down inner electron (artificial spin-selective case; dashed).
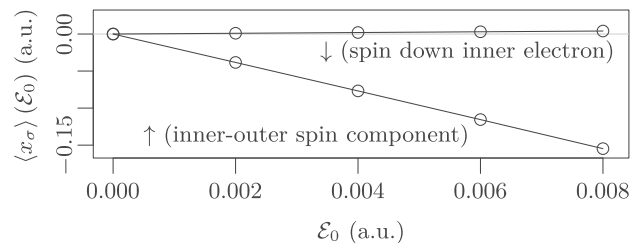

FIG. 7. Dipole expectation values for both spin components of the Li model in the presence of a constant electric field with field strength $\mathcal{E}_0$ ("seen" by all electrons). The inner-outer spin component is displaced in the direction opposite to the electric field, as expected for negatively charged particles. The displacement of the opposite-spin component (corresponding to the spin-down inner electron here) is in the same direction as the electric field, as a response to the outer electron.

D. Ionization rates obtained with different SAE and TDDFT approximations with and without SIC

After having obtained insight into the role of inner electrons in ionization and polarization from *ab initio* solutions of the TDSE, results from full TDDFT and frozen-core calculations are presented and interpreted in this section. The SAE approximation, as explained in Sec. III F, is also counted as an FCA in which only the KS valence orbital is propagated in the frozen ground state KS potential (plus the potential due to the laser). The SAE results do not suffer from self-interaction introduced during the propagation of orbitals in time. However, a self-interaction error may originate from the ground state KS potential.

For two approximations we considered, the results have been so unreasonable that they are not even shown here but are just mentioned. First, the pure LDA TDDFT approach completely fails in generating a reasonable behavior of ionization probability vs time in the multiphoton regime $\omega < E_{\rm ip}$ so that a rate $p_\omega(t) \simeq 1 - \exp(-\Gamma_\omega t)$ could not be extracted. Second, the TDDFT approach using PZ SIC leads to resonances of inner electrons at high frequencies $\omega > 0.8$, leading to a nonmonotonous behavior of the ionization rate not seen in the exact result.

1. SAE results

Ionization rates from SAE calculations in which frozen KS potentials were used are shown in Fig. 8(a). In the low-frequency regime $\omega < 0.2$ both SAE ionization rates change rapidly with the frequency, as the exact result does due to the many avoided crossings discussed in Sec. IV B 3. To the right of the two-photon ionization peak a sharp minimum at $\omega_{\rm min} \in [0.2, 0.26]$ shows up in all results. In the remaining multiphoton ionization part up to $\omega = E_{\rm ip} \simeq 0.4$ one or two peaks are visible, corresponding to one-photon excited-state-assisted ionization.

The LDA SAE approach yields too few peaks and an incorrect curvature around $\omega \simeq 0.25$. Furthermore, the excited-state-assisted ionization peak around $\omega \simeq 0.31$ is blueshifted, while the ionization threshold is redshifted. This can be partially explained by the wrong asymptotic behavior of the KS potential originating from self-interaction in pure LDA. The SAE approximation in the PZ-corrected case leads to the correct number of peaks. If each of the n-photon peaks is shifted to the right by $\Delta\omega \simeq \frac{0.04}{n}$ one finds a striking agreement with the exact TDSE result with respect to peak positions, widths, and heights. This improvement over pure LDA is due to the asymptotically correct KS potentials in the case of PZ SIC. In fact, three-dimensional DFT calculations applying the PZ SIC are often useful to quantitatively reproduce experimental values for ionization thresholds and excitation energies. Hence, the required shift $\Delta\omega$ may be due to the one-dimensionality of the Li model system considered in this work.

In the single-photon ionization regime $\omega > E_{\rm ip}$ a monotonic decrease of the ionization rate, starting from its maximum value for $\omega \simeq E_{\rm ip}$, is observed. However, a convex curvature as for the spin-selective laser gedanken experiment arises. Hence, all approaches neglecting inner electron dynamics completely (pure LDA SAE and PZ-corrected SAE) or partially (spin-selective laser gedanken experiment) yield a convex curvature

in the logarithmic plot, presumably because the antiscreening effect is neglected.

2. Full TDDFT results

Ionization rates from the full TDDFT calculations are shown in Fig. 8(b). As mentioned above, plain LDA TDDFT does not allow one to extract a rate in the multiphoton ionization regime at all. Compared to the SAE results, the PZ TDDFT rate in the multiphoton ionization regime appears to be calculated with less spectral resolution. This is expected because "unfrozen" KS potentials do not support stationary energy levels that could aid ionization via resonant excitations.

In the single-photon regime the full TDSE and the LDA TDDFT calculations yield an exponential decrease of the ionization rate for increasing photon energies. The corresponding slopes approximately equal each other. However, the rate predicted by LDA TDDFT is too high. A possible explanation for the overestimated rate is the following: the *down*shift of the KS energy during ionization in LDA without SIC (see Sec. IV E below) leads to an *increased* ionization probability in the single-photon regime (because the ionization probability drops with increasing excess energy $\omega - E_{\rm ip}$). Hence, one may view the LDA rate as rather being blueshifted than upshifted.

Surprisingly, the PZ-corrected TDDFT calculations yield the worst rate, which is too small at the threshold, decreases too rapidly with increasing ω, and has a concave curvature. The reason for this wrong behavior is discussed in Sec. IV F below.

Concluding this section, we can state that none of the considered approximations is able to yield correct ionization rates over the frequency interval [0.1, 1.0], the best performing being the LDA PZ-SIC SAE approximation in the multiphoton and the pure LDA TDDFT in the single-photon ionization regime.

E. Importance of SIC for resonances in the multiphoton regime

The PZ SIC leads to "better" KS energies of the populated levels in the sense of being closer to the respective ionization energies. The energies of the unpopulated levels in the ground state KS potential also benefit from the SIC, leading to "better" excitation energies. Both are important ingredients for a correct ionization rate in the multiphoton regime. Moreover, in a time-dependent calculation SIC also helps taking into account the discontinuity of the KS potential at integer orbital occupation numbers (this is the so-called "derivative discontinuity" in the XC energy, cf. [36]). The ionization potential must not depend on the ionization probability $p(t)$. Hence, the KS energy of the orbital from which predominantly ionization occurs should be independent of $p(t) \in [0,1)$. Only when $p(t) = 1$ is reached, the KS potential, and thus the orbital energy, should change discontinuously. The single-particle density in the vicinity of the nucleus decreases as $p(t)$ increases. As a result, the repulsive Hartree potential is weakened so that all orbital energies would shift to lower values if the XC potential did not counteract. In fact, pure LDA does not counteract properly so that the KS level energies vary continuously with $p(t)$. PZ SIC implements the derivative discontinuity, at least
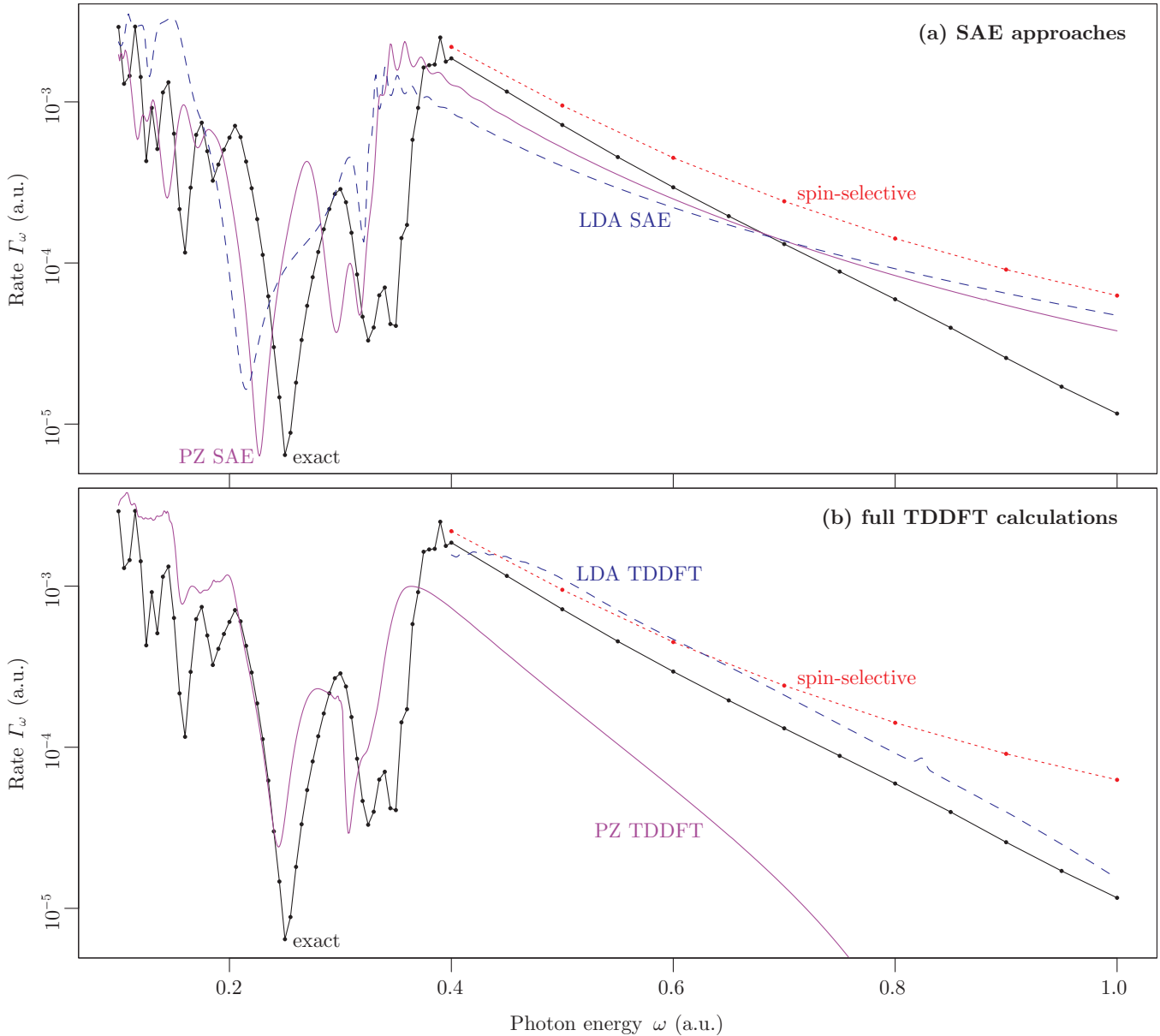
FIG. 8. (Color online) Ionization rate Γ_ω obtained by SAE approaches (a) and by full TDDFT calculations (b). For reference, in both panels the result from the exact TDSE (labeled "exact," drawn solid with bullets) and the "spin-selective" TDSE calculation (dotted with bullets) in the single-photon regime $\omega > 0.4$ where it is different from the full calculation (see Fig. 5) are included. The SAE results in (a) are labeled "LDA SAE" (i.e., SAE with frozen LDA ground state KS potential; dashed) and "PZ SAE" (i.e., SAE with frozen LDA PZ-SIC ground state KS potential; solid). The full TDDFT results in (b) are labeled "LDA TDDFT" (dashed) and "PZ TDDFT" (i.e., LDA with PZ SIC; solid). LDA TDDFT results are omitted in the multiphoton regime $\omega < 0.4$, and PZ TDDFT in the high-frequency regime $\omega > 0.8$, because a single-ionization rate cannot be determined in these cases.

approximately. This is illustrated in Fig. 9 for a valence KS orbital occupation $n_{\text{val}} \in [0,1]$ for pure LDA and PZ SIC applied to LDA. By considering fractional occupations in the stationary ground state calculations we are mimicking adiabatically evolving ionization, i.e., $1 - n_{\text{val}} = p$ with p the instantaneous ionization probability.

For the neutral atom ground state $n_{\text{val}} = 1$ the PZ SIC lowers the valence orbital energy compared to the uncorrected LDA case,

$$-0.355 = \varepsilon_{\text{val}}^{(\text{PZ})}(1) < \varepsilon_{\text{val}}^{(\text{LDA})}(1) = -0.329. \qquad (27)$$

In the Li$^+$ limit $n_{\text{val}} = 0$ both approaches almost agree,

$$-0.671 = \varepsilon_{\text{val}}^{(\text{PZ})}(0) \simeq \varepsilon_{\text{val}}^{(\text{LDA})}(0) = -0.672. \qquad (28)$$

In pure LDA the orbital energy shifts almost linearly during ionization down to small values of n_{val}. With PZ SIC the orbital energy is shifted much less during ionization as long as $n_{\text{val}} > 0.2$. In the region $n_{\text{val}} \in [0,0.2]$ the PZ-SIC orbital energy describes a "smoothed jump" down to the Li$^+$ value. Hence, we find that the PZ SIC smoothes the step-function-like behavior the unknown, exact SIC would yield. The improvement over
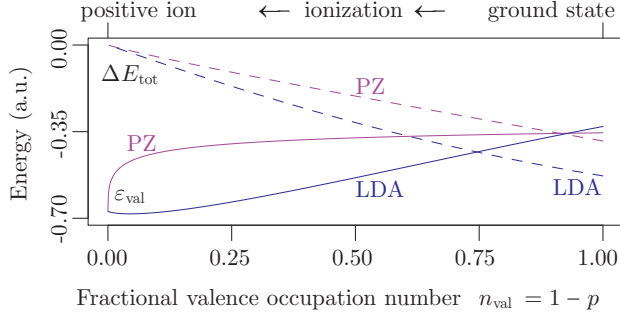
FIG. 9. (Color online) Orbital energy of the "valence" KS orbital ε_{val} (solid) and the total energy difference ΔE_{tot} (dashed) vs the fractional valence occupation number $n_{\text{val}} = 1 - p$, where p is the ionization probability, for pure LDA and for LDA with PZ SIC.

pure LDA regarding the constancy of the orbital energy of the "ionizing KS level" is essential.

F. Problem of LDA PZ SIC in single-photon ionization

With all the benefits from PZ SIC concerning KS level energies and the asymptotic behavior of the KS potential, it is an obvious question why PZ-corrected LDA fails so badly in the single-photon ionization regime. The gedanken experiment in Sec. IV C indicates that dynamical coupling effects between electrons such as antiscreening become increasingly important as the photon energy ω rises. In TDDFT, the coupling between KS orbitals is mediated by the Hartree part and the XC part of the KS potential. With PZ SIC the orbital-dependent KS potential reads

$$v_i(x) = v(x) + v^{(\text{LDA})}[n_{\sigma_i}](x) + v^{(\text{H})}[n](x)$$
$$- v^{(\text{LDA})}[n_i](x) - v^{(\text{H})}[n_i](x). \quad (29)$$

The Hartree potential is a linear functional of the total electron density so that

$$v_i(x) = v(x) + v^{(\text{LDA})}[n_{\sigma_i}](x)$$
$$- v^{(\text{LDA})}[n_i](x) + v^{(\text{H})}[n - n_i](x). \quad (30)$$

The effective Hartree term $v^{(\text{H})}[n - n_i](x)$ for the valence KS orbital after SIC is solely determined by the core KS orbital density. As a result, antiscreening is stronger than without SIC of the Hartree potential. The SIC of the LDA part acts in the opposite direction. However, the SIC to the LDA XC potential is not exact, so that a net overestimated antiscreening may remain, leading to a lower ionization rate at higher photon energies. Moreover, the dependence of the PZ TDDFT ionization rate as a function of the laser frequency is wrong in Fig. 8(b), pointing to a deficiency in the *dynamics* of the XC potential (note that the PZ SAE rate bends in the *opposite* direction).

The fact that pure LDA leads at least to the correct slope of the ionization rate in the single-photon ionization regime is thus likely due to a lucky cancellation of errors, i.e., the suppressed antiscreening is compensated by the error in the LDA XC potential at all frequencies $\omega \in [0.5, 1]$.

V. CONCLUSION AND OUTLOOK

In this work, we benchmarked various density-functional-based approximate approaches to laser ionization with a numerically exactly solvable three-electron model atom.

In the apparently simple photoeffect regime where only one photon is required for ionization, a surprisingly pronounced dependence of the ionization dynamics on the correct treatment of the inner electrons is found. These inner electrons are usually assumed to be passive, justifying frozen-core, single-active-electron, and pseudopotential approaches. However, because of the opposite time scales of inner and outer electrons with respect to the laser period *antiscreening* of the nuclear charge by the inner electrons occurs, which is ignored in such approaches (but could be modeled by a dynamical polarization potential). For instance, frozen-core orbitals lead to ionization rates too high, with an erroneously curved slope of the ionization rate as a function of the laser frequency. Unfortunately, the more advanced Perdew-Zunger self-interaction-corrected local density approximation fails as well at high frequencies because of an overemphasized antiscreening.

In order to correctly describe ionization in the multiphoton domain, energy levels as well as dipole transition probabilities must be reproduced by the simulation method, which is very demanding for pseudopotential and single-active-electron approaches. Moreover, the energy levels should not change as excited states get populated because this would move the system out of resonance. On the other hand, it is known that once the population is inverted, the density is the ground state density of a "new," discontinuously changing Kohn-Sham potential [12,37]. Only proper self-interaction-free Kohn-Sham potentials may capture such multiphoton ionization effects involving resonances. We found that the Perdew-Zunger self-interaction-corrected local density approximation performs well for the lithium model atom in this respect, at least qualitatively.

In future work, it is worth comparing our exact numerical model Li results with Kohn-Sham results using more advanced exchange-correlation functionals than we did in the current work [38]. There might well be exchange-correlation potentials "out there" that perform well in both the multiphoton and single-photon ionization regimes.

APPENDIX: NUMERICAL SOLUTION OF THE THREE-PARTICLE TDSE

In this Appendix, numerical details concerning the solution of the TDSE (20) are given. The full solution of the three-particle TDSE for processes involving ionization is numerically demanding even if the spatial degrees of freedom are reduced to one per particle. For that reason a Cartesian TDSE solver in three dimensions (i.e., one per particle) was implemented on a graphics processing unit (GPU) using the NVIDIA CUDA [39] platform. The solver is highly optimized

for the purpose of this paper. A speedup of three orders of magnitude over a single-core CPU implementation covering the full three-dimensional Cartesian grid is achieved on a desktop computer featuring a NVIDIA GeForce GTX 580 GPU. The speedup originates equally from an efficient implementation utilizing the high single-precision performance of the GPU and the adjustment of the simulation grid. "Mixed precision" techniques allow one to obtain results in double precision although most of the numerical effort consists of single-precision floating point operations.

The kinetic energy operator is discretized using the implicit Numerov expression, which is accurate up to fourth order in the spatial grid spacing Δx. For the propagation in time we employ the unitary Crank-Nicolson method consisting of an (explicit) forward and an (implicit) backward step, accurate up to second order in the time step Δt. The explicitly time-dependent Hamiltonian $H(t)$ is evaluated at midpoints $\tau = t + \frac{\Delta t}{2}$.

The linear equations to propagate the discretized wave function in time for one time step can easily be arranged to require the solution of no more than a single implicit equation with a $3 \times 3 \times 3$ stencil. For a sufficiently small time step Δt the corresponding coefficient matrix is diagonal dominant. Hence, the Jacobi method can be used to determine its solution. Faster convergence of long-wavelength errors is achieved by applying a multigrid scheme. Finally, a high throughput of floating point operations is obtained by using mixed precision techniques and different data caching stages combined with massive parallelization.

The numerical grid was optimized, exploiting what is known about the probability density dynamics during long-wavelength, single ionization. Recall that the laser is tuned such that solely the outer electron is removed from the atom. As a consequence, the single spin-down inner electron is tightly bound to the core at all times. This means that $|\phi_{23}(t;x_1,x_2,x_3)|^2$ will only yield nonvanishing probabilities for small $|x_1|$. Hence, one may choose a small box size in the x_1 direction. In contrast to that, the inner-outer spin component in the x_2 and x_3 directions may be spatially extended. However, if both $|x_2|$ *and* $|x_3|$ are large,

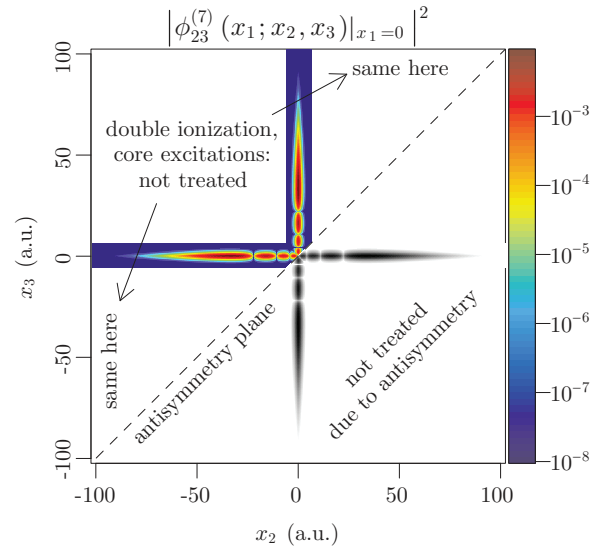FIG. 10. (Color online) Spin-resolved probability density $|\phi_{23}^{(7)}(x_1,x_2,x_3)|^2$ of the seventh excited state cut at $x_1 = 0$. The adapted grid omits those regions with a white background.

$|\phi_{23}(t;x_1,x_2,x_3)|^2$ must be *negligible* for the allowed laser parameters, i.e., those that do *not* lead to double (or triple) ionization. Consequently, the grid regions where $|x_2|$ *and* $|x_3|$ are large are omitted. Finally, by making use of the antisymmetry $\phi_{23}(t;x_1,x_2,x_3) = -\phi_{23}(t;x_1,x_3,x_2)$ only the region $x_2 \leqslant x_3$ needs to be considered numerically.

Denoting the width of an ionization channel in grid points by N_{small} and its total length by N_{large}, the total number of grid points compared to an $N_{\text{small}} \times N_{\text{large}} \times N_{\text{large}}$ cuboid is reduced by a factor of $2N_{\text{large}}/N_{\text{small}}$. The results presented in this work have been checked to be converged for $N_{\text{small}} = 64$ and $N_{\text{large}} = 1024$ (for $\Delta x = 0.2$ and $\Delta t = \Delta x/8$), which corresponds to a speedup of 32 caused by the grid adjustment alone. As an example, the probability density $|\phi_{23}^{(7)}(x_1 = 0,x_2,x_3)|^2$ of the seventh excited state on the optimized grid is shown in Fig. 10.

[1] R. G. Parr and W. Yang, *Density Functional Theory of Atoms and Molecules* (Oxford Science Publications, New York, 1989).

[2] R. M. Dreizler and E. K. U. Gross, *Density Functional Theory: An Approach to the Quantum Many-Body Problem* (Springer, Berlin/Heidelberg, 1990).

[3] E. Engel and R. M. Dreizler, *Density Functional Theory: An Advanced Course* (Springer, Berlin/Heidelberg, 2011).

[4] W. Kohn and L. J. Sham, Phys. Rev. **140**, A1133 (1965).

[5] L. Szasz, *Pseudopotential Theory of Atoms and Molecules* (Wiley, New York, 1985).

[6] F. Nogueira, A. Castro, and M. Marques, in *A Primer in Density Functional Theory*, edited by C. Fiolhais, F. Nogueira, and M. Marques, Lecture Notes in Physics Vol. 620 (Springer, Berlin/Heidelberg, 2003), pp. 218–256.

[7] M. A. L. Marques, N. T. Maitra, F. M. S. Nogueira, E. K. U. Gross, and A. Rubio, *Fundamentals of Time-Dependent Density Functional Theory*, Lecture Notes in Physics Vol. 837 (Springer, Berlin/Heidelberg, 2012).

[8] C. Ullrich, *Time-Dependent Density-Functional Theory: Concepts and Applications* (Oxford University Press, New York, 2012).

[9] C. A. Ullrich, J. Chem. Phys. **125**, 234108 (2006).

[10] P. Hessler, N. T. Maitra, and K. Burke, J. Chem. Phys. **117**, 72 (2002).

[11] Y. Kurzweil and R. Baer, Phys. Rev. B **73**, 075413 (2006).

[12] N. T. Maitra, K. Burke, and C. Woodward, Phys. Rev. Lett. **89**, 023002 (2002).

[13] M. Protopapas, C. H. Keitel, and P. L. Knight, Rep. Prog. Phys. **60**, 389 (1997).

[14] D. B. Milošević, G. G. Paulus, D. Bauer, and W. Becker, J. Phys. B **39**, R203 (2006).

[15] K. C. Kulander, K. J. Schafer, and J. L. Krause, Int. J. Quantum Chem. **40**, 415 (1991).

[16] M. Awasthi, Y. V. Vanne, A. Saenz, A. Castro, and P. Decleva, Phys. Rev. A **77**, 063403 (2008).

[17] O. Smirnova, Y. Mairesse, S. Patchkovskii, N. Dudovich, D. Villeneuve, P. Corkum, and M. Y. Ivanov, Nature (London) **460**, 972 (2009).

[18] A. E. Boguslavskiy, J. Mikosch, A. Gijsbertsen, M. Spanner, S. Patchkovskii, N. Gador, M. J. J. Vrakking, and A. Stolow, Science **335**, 1336 (2012).

[19] R. Grobe and J. H. Eberly, Phys. Rev. Lett. **68**, 2905 (1992).

[20] C. Ruiz, L. Plaja, and L. Roso, Phys. Rev. Lett. **94**, 063002 (2005).

[21] Had we chosen the Li configuration $S = 1/2$ and $M_S = -1/2$ instead of $M_S = +1/2$, the role of single-particle spin-up and spin-down components would be reversed, of course.

[22] C. J. Joachain, N. J. Kylstra, and R. M. Potvliege, *Atoms in Intense Laser Fields* (Cambridge University Press, Cambridge, 2012).

[23] S.-I. Chu and D. A. Telnov, Phys. Rep. **390**, 1 (2004).

[24] P. Hohenberg and W. Kohn, Phys. Rev. **136**, B864 (1964).

[25] E. Runge and E. K. U. Gross, Phys. Rev. Lett. **52**, 997 (1984).

[26] J. P. Perdew and A. Zunger, Phys. Rev. B **23**, 5048 (1981).

[27] Rigorously speaking, the fictitious KS particles should not be viewed as "real" electrons. However, it seems not unreasonable to take the valence KS orbital as the starting point for a SAE calculation.

[28] H. G. Muller, Phys. Rev. A **60**, 1341 (1999).

[29] C.-T. Chen and F. Robicheaux, Phys. Rev. A **54**, 3261 (1996).

[30] M. Meckel, D. Comtois, D. Zeidler, A. Staudte, D. Pavičić, H. C. Bandulet, H. Pépin, J. C. Kieffer, R. Dörner, D. M. Villeneuve, and P. B. Corkum, Science **320**, 1478 (2008).

[31] P. Mulser and D. Bauer, in *High Power Laser-Matter Interaction*, Springer Tracts in Modern Physics Vol. 238 (Springer-Verlag, Berlin/Heidelberg, 2010), pp. 267–330.

[32] Note, however, that all methods used in this work can be applied to the nonperturbative regime as well. We restrict ourselves to rather small field strengths here for purely methodical reasons.

[33] V. Kapoor and D. Bauer, Phys. Rev. A **85**, 023407 (2012).

[34] Z. Zhao and J. Yuan, Phys. Rev. A **89**, 023404 (2014).

[35] B. Zhang, J. Yuan, and Z. Zhao, Phys. Rev. Lett. **111**, 163001 (2013).

[36] J. P. Perdew, R. G. Parr, M. Levy, and J. L. Balduz, Phys. Rev. Lett. **49**, 1691 (1982).

[37] M. Ruggenthaler and D. Bauer, Phys. Rev. Lett. **102**, 233001 (2009).

[38] S. Kümmel and L. Kronik, Rev. Mod. Phys. **80**, 3 (2008).

[39] NVIDIA Corporation, Parallel programming and computing platform|cuda|nvidia, http://www.nvidia.com/cuda/, 2013.